Article

Boosting a practical lithium carbon dioxide battery through a decoupled electrolyte

Fangli Zhang[1], Jodie A. Yuwono [1], Ruizhi Zhang[1], Lars Thomsen [2], Shuixin Xia[1,3], Wenchao Zhang [4] ✉, Liyuan Chai[4] & Zaiping Guo [1,5] ✉

Highly conductive electrolytes and stable electrolyte|electrode interfaces are desired for next-generation batteries. Constructing solid-electrolyte interphases on electrodes is a prevailing strategy for enhancing interfacial stability but fails to prevent inevitable breakdown and reformation of interphases during prolonged cycling. Herein, a decoupled electrolyte is designed by introducing a co-solvent (tetraethylene glycol dimethyl ether) with high stability and high positive electrostatic potential values into highly conductive dimethylformamide-based electrolytes, which suffer from electrolyte|positive electrode instability. The preferential adsorption of cations solvated with co-solvents on the positive electrode during discharge induces the formation of a co-solvent-rich localized environment, inhibiting side reactions and contributing to long cyclability. Meanwhile, dimethylformamide in the bulk electrolyte helps to maintain high ionic conductivity, thus improving kinetics. Notably, lithium-carbon dioxide cells with this decoupled electrolyte demonstrate a significantly improved cycle life of ~ 2600 hours and a low overpotential of ~ 1 V, even with a metal-free commercial reduced graphene oxide catalyst. Our work provides an alternative strategy to solid-electrolyte interphase construction for stabilizing electrolyte|electrode interface and unlocks the potential of previously underexplored solvents in batteries.

The increasing demand for portable electronics has spurred intensive research into developing batteries with high energy density and fast-charging capability. The electrolyte, a crucial component of batteries, plays a critical role in determining power density by governing ion transport, necessitating high ionic conductivity[1–3]. Furthermore, the electrolyte|electrode interfaces, where electrochemical reactions occur, largely dictate the reversibility and cycling stability of batteries, requiring highly stable interfaces[4]. Thus, an ideal electrolyte must inherently satisfy both these requirements simultaneously.

To stabilize electrolyte|electrode interfaces, past research has often focused on tailoring electrolyte structures to construct a solid-electrolyte interphase (SEI) on electrodes by employing strategies such as high-concentration electrolytes, dual-salt electrolytes, fluorinated solvents, or electrolyte additives[5–8]. However, these strategies often decrease ionic conductivity, sacrificing the advantage of fast ion transport within bulk electrolytes[9–11]. Additionally, the inevitable volume variations of electrodes during cycling lead to cracking in SEI layers, resulting in their uncontrollable breakdown and reparation. This dynamic process leads to low Coulombic efficiency (CE) and capacity fading over prolonged cycling[12,13]. Notably, interfacial instability is pronounced in gas-involved batteries, such as metal-O_2 and metal-CO_2 batteries, due to the generation of highly reactive intermediates like O_2^- and CO_2^{2-} on the positive electrode surface during multiphase reactions[14]. SEI layers, unfortunately, fail to block

[1]School of Chemical Engineering and Advanced Materials, The University of Adelaide, Adelaide, SA, Australia. [2]Australian Synchrotron, Australian Nuclear Science and Technology Organization, Melbourne, VIC, Australia. [3]School of Materials and Chemistry, University of Shanghai for Science and Technology, Shanghai, China. [4]School of Metallurgy and Environment, Central South University, Changsha, China. [5]Department of Materials Science and Engineering, City University of Hong Kong, Kowloon, Hong Kong, China. ✉e-mail: wenchao.zhang@csu.edu.cn; zaiping.guo@adelaide.edu.au

side reactions between these intermediates and the electrolyte, resulting in unstable interface layers that lead to poor cycling performance. To ensure the success of next-generation batteries, it is essential to design a decoupled electrolyte capable of forming chemically and electrochemically stable electrolyte|electrode interfaces to inhibit side reactions while maintaining high conductivity in the bulk electrolyte.

In this work, Li-CO_2 batteries serve as a test platform to demonstrate how a decoupled electrolyte functions and improves battery performance. Compared to conventional solvents, tetraethylene glycol dimethyl ether (TEGDME) and dimethyl sulfoxide (DMSO), which are commonly used in metal-CO_2 batteries, dimethylformamide (DMF) presents a promising alternative due to its low viscosity, high ionic conductivity, and weak electrostatic interaction with cations owing to its low-polarity alkyl groups[15–18]. These properties facilitate ion migration and the desolvation process, improving battery kinetics and rate capability. However, DMF suffers from interfacial instability caused by its high reactivity with reduced oxygen species[19]—key intermediates involved in the electrochemical reactions—on the positive electrode. This leads to parasitic reactions, irreversible electrolyte consumption, and poor cycling performance.

Herein, we design a decoupled electrolyte that combines highly conductive bulk properties of DMF with an inert localized environment near the positive electrode. The electric double layer (EDL), a dynamic region at the electrolyte|electrode interface where ions and solvents accumulate during cycling, plays a critical role in shaping the interfacial chemistry and electrochemical environment. However, which solvation structures and why these solvation structures preferentially de-solvate at the EDL and adsorb onto the electrode surface —thus influencing the stability of the electrolyte|electrode interface— are essential but not well understood so far. An electrostatic potential (ESP) of a solvated cation reflects the spatial distribution of charge around the cation and its coordinating solvent molecules[20–22]. Through theoretical calculations, we reveal that during discharge, solvated cations with relatively high positive ESP values preferentially adsorb onto the positive electrode surface. This finding guides us to introduce a low concentration of the co-solvent TEGDME into DMF-based electrolytes to regulate solvation structures and their ESP values, finally tailoring the preferential adsorption of TEGDME onto the positive electrode surface. TEGDME possesses high ESP values, high stability towards reduced oxygen species, strong coordination with cations, and high CO_2 solubility. These properties enable Li^+ ions solvated with TEGDME to exhibit higher positive ESP values than those solvated with DMF, creating an inert, TEGDME-rich localized environment near the positive electrode. This environment effectively suppresses DMF-related side reactions, as illustrated in Fig. 1. Meanwhile, highly conductive DMF remains in the bulk electrolyte, ensuring favourable rate capability for the batteries. With this decoupled electrolyte, Li-CO_2 cells achieved improved electrochemical performance, delivering a prolonged cycle life of ~2600 h and a small overpotential of ~1 V, even with a metal-free commercial reduced graphene oxide (rGO) catalyst. Such a design of decoupled electrolytes—modulating the solvation structure through ESP distribution to guide selective interfacial adsorption of a stable co-solvent—can be extended to other battery systems that face similar interfacial issues, such as metal-air or high-voltage lithium-ion batteries.
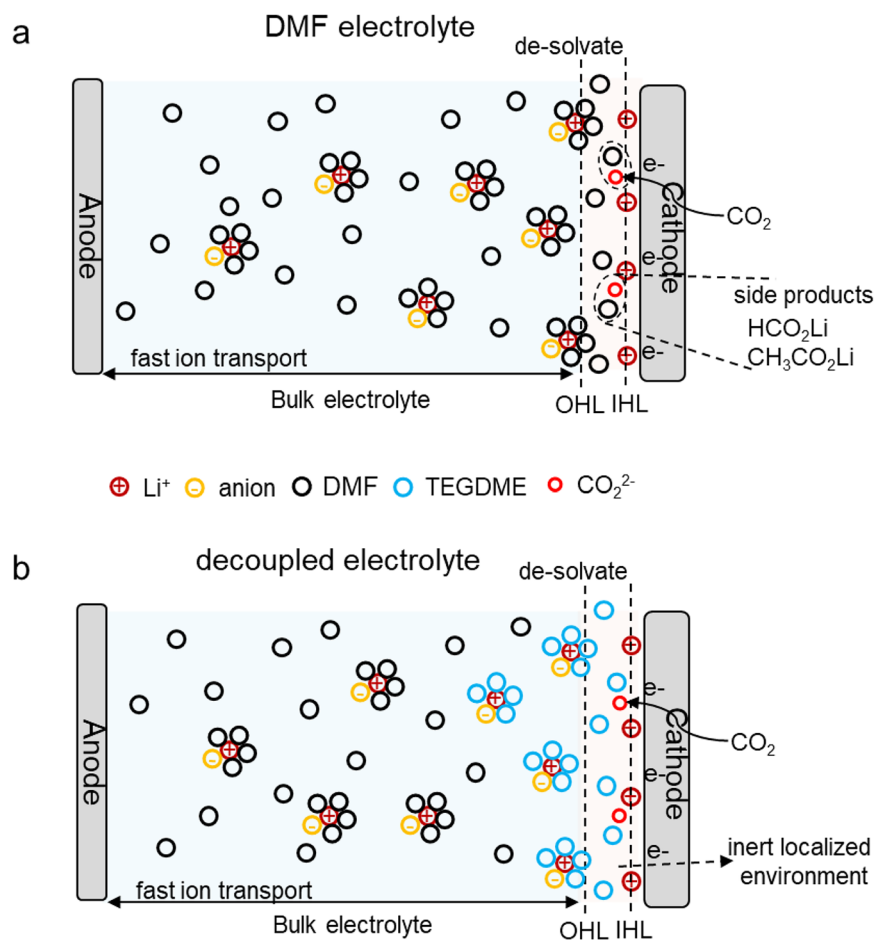
Results

Current bottleneck and decoupled electrolyte design
The commonly solvents in Li-CO_2 batteries, TEGDME and DMSO, possess high viscosity and low ionic conductivity, resulting in sluggish battery kinetics and a large polarization. Therefore, it is necessary to explore alternative solvents. DMF stands out as a promising candidate owing to its considerably lower viscosity (Fig. 2a) and higher ionic conductivity (Fig. 2b) compared to TEGDME and DMSO, enabling

enhanced ion transport in the bulk electrolyte and improved wettability on the porous positive electrode surface. Additionally, as shown in Fig. 2c, the low-polarity alkyl groups of DMF contribute to a weaker Li-DMF binding energy (-51.86 kcal mol^{-1}) compared to strong Li-DMSO coordination (-73.05 kcal mol^{-1}), which facilitates both Li^+ diffusion and the desolvation process at the electrolyte|electrode interface[23]. These features of DMF ensure reduced battery impedance and increased battery kinetics.

To evaluate the battery performance of Li-CO_2 cells using different solvents, all electrolytes were prepared with 1 M lithium bis(fluorosulfonyl)imide (LiFSI) dissolved in a single solvent. As expected, the cell employing the 1 M LiFSI/DMF electrolyte (denoted as DMF cell) delivered the lowest charging potential of ~3.8 V (Fig. 2d) and the smallest overpotential of ~1 V (Fig. 2e), highlighting its merits in reducing polarization and enhancing kinetics for CO_2 reduction/evolution reactions (CRR/CER). Beyond facilitating fast ion transport (Fig. 2b), the DMF cell presented notably lower impedances compared to the cells using the 1 M LiFSI/DMSO and 1 M LiFSI/TEGDME electrolytes (denoted as DMSO cell and TEGDME cell, respectively) (Supplementary Fig. 1), indicating reduced reaction resistance and improved kinetics for the interfacial charge-transfer process[24,25]. The advantages of DMF were further evidenced by its full discharge-charge capability and rate performance[26,27]. The DMF cell achieved a large full-discharge capacity of 13,350 mAh g^{-1} with a low overpotential of 1.2 V, while the DMSO cell delivered a capacity of only 8,629 mAh g^{-1} with a high overpotential of 1.62 V (Supplementary Fig. 2), indicating the great effect of DMF on promoting CRR. Additionally, the DMF cell demonstrated enhanced rate capability (Fig. 2f and Supplementary Fig. 3), with a significantly reduced charging potential compared to DMSO and TEGDME cells across all current densities, suggesting a lower energy barrier for CER. However, despite the improved battery kinetics offered by DMF, its instability was observed during cycling, with sudden cell failure occurring at the 73rd cycle (Fig. 2d). This limits the application of DMF in Li-CO_2 batteries.

To reveal the origin of the instability of the DMF electrolyte, the linear sweep voltammetry was first employed to test its stability towards lithium metal. The leakage current in Li‖Ti cells using the DMF electrolyte revealed a negligible leakage current up to 6 V (V vs. Li|Li$^+$) (Supplementary Fig. 4), reflecting its high stability towards lithium negative electrodes, even at high potential[28]. This offers a clue that the instability of the DMF cell may originate from the positive electrode side. In Li-CO_2 batteries, *CO_2^{2-} radicals occur at the electrolyte|positive electrode interface during discharge, as key intermediates involved in the multi-step CRR[14,26,29–31]. Based on previous studies, DMF was found to possess high chemical reactivity towards reduced oxygen species, which triggers uncontrollable side reactions and generate side products (HCO_2Li/CH_3CO_2Li)[19]. To examine the occurrence of side reactions between DMF and *CO_2^{2-}, Li-CO_2 cells were disassembled after discharge to check the discharge product and side products formed on the positive electrode. First, the formation of discharge product Li_2CO_3.was confirmed by the selected area electron diffraction (SAED) pattern, where the diffraction rings correspond to the (11$\bar{2}$), (51$\bar{1}$), and (330) planes of Li_2CO_3 (Supplementary Fig. 5), and the C 1s spectra obtained through X-ray photoelectron spectroscopy (XPS)[32] (Supplementary Fig. 6). Following that, ex-situ Fourier transform infrared (FTIR) spectroscopy was employed to identify side products. Figure 2g shows that new peaks emerged at ~1380 and 1600 cm^{-1} after discharge, assigned to HCO_2Li/CH_3CO_2Li, which proves the occurrence of side reactions between DMF and *CO_2^{2-} (Fig. 2h)[19,33]. After charge, the peaks of HCO_2Li/CH_3CO_2Li disappeared while the peaks of Li_2CO_3 still remained, indicating that the side products decompose prior to Li_2CO_3 due to their lower oxidation barriers. Unfortunately, the formation and decomposition of HCO_2Li/CH_3CO_2Li are irreversible and accompany by CO_2 and H_2O evolution[19,33–35], resulting in unsatisfactory CE and poor cycling stability, as evidenced
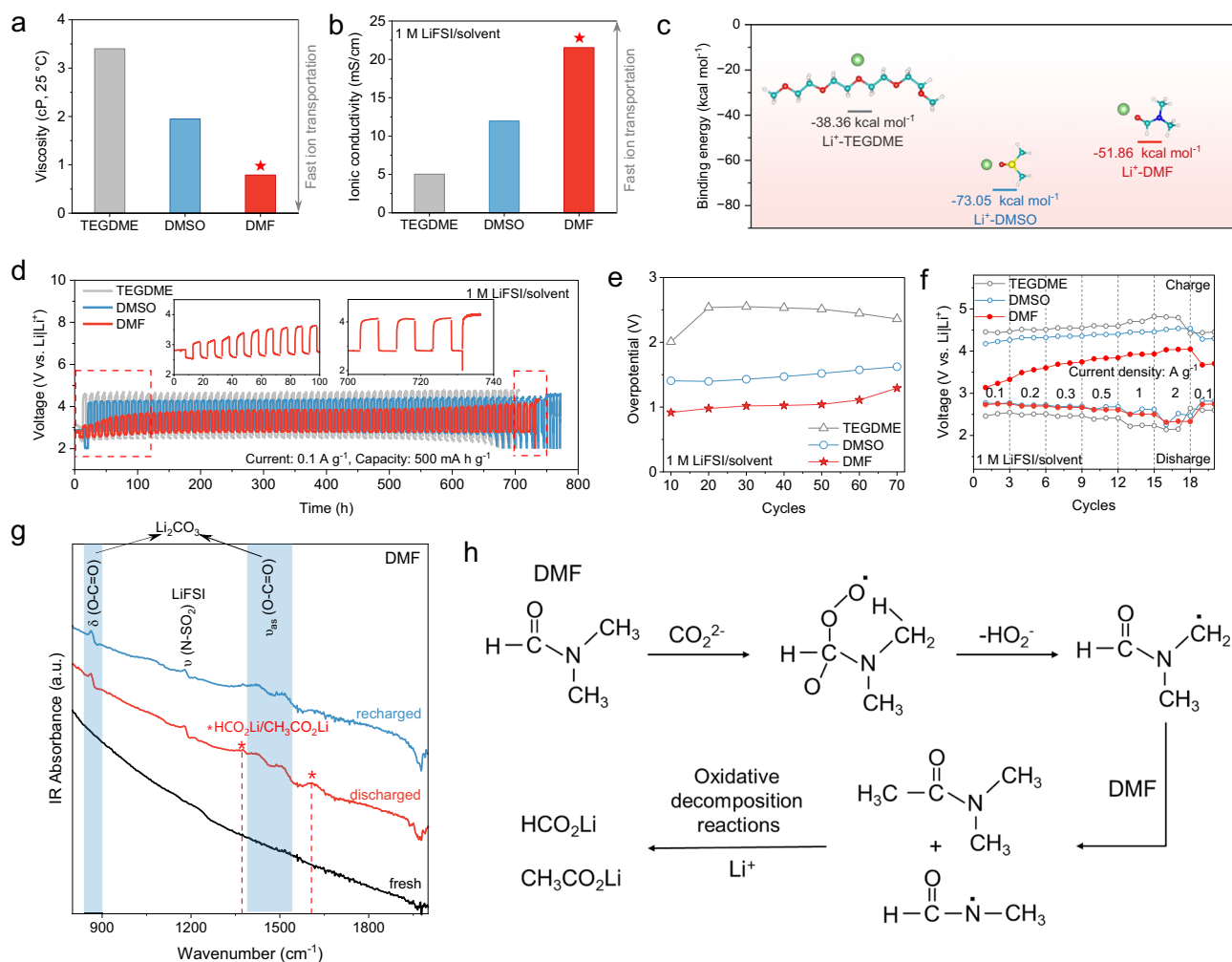
Fig. 1 | Schematic illustrations of the bulk electrolyte and the electric double layer (EDL) structure. The EDL includes the inner Helmholtz layer (IHL) and the outer Helmholtz layer (OHL), during discharge. EDL is an interfacial region between the electrode and the bulk electrolyte, where electrical charges are spatially distributed. It consists of two sublayers: IHL and OHL. The IHP is the inner layer of the EDL on the electrode surface, which determines the competitive adsorption of cations, anions, and solvent molecules near the electrode surface, thus being strongly associated with the electrolyte|electrode interfacial stability and the formation of SEI layers. The OHL is positioned farther from the electrode surface than the IHL and primarily comprises solvated cations[67–69]. **a** In the bare DMF electrolyte, side reactions between DMF and CO_2^{2-} on the positive electrode surface result in the formation of irreversible side reaction products (HCO$_2$Li/ CH$_3$CO$_2$Li). **b** The inert, TEGDME-rich localized environment near the positive electrode surface in the decoupled electrolyte inhibits side reactions, enhancing interfacial stability and maintaining high conductivity in the bulk electrolyte.

by the electrochemical performance of the DMF cell (Fig. 2d). Electrochemical impedance spectroscopy (EIS) analysis further confirmed the interfacial instability in the DMF cell, showing a significant increase in impedance after the first discharge-recharge cycle (Supplementary Fig. 7).

The key to overcoming the limitations of DMF is to design a decoupled electrolyte, which minimizes the contact between DMF and $*CO_2^{2-}$ at the electrolyte|positive electrode interface while preserving its high conductivity in the bulk electrolyte. During discharge, the electric field naturally attracts electrolyte components with positive ESP values to adsorb onto the positive electrode surface. Theoretically, different solvation structures of Li$^+$ ions lead to differences in ESP values, causing Li$^+$ ions with the most positive ESP values and their solvated solvents to preferentially accumulate near the positive electrode, where they contact with $*CO_2^{2-}$. Based on this insight, we introduced a co-solvent with strong coordination with Li$^+$ ions and high stability against $*CO_2^{2-}$ into DMF-based electrolytes to manipulate Li$^+$ solvation structures and direct the preferential adsorption of solvents onto the positive electrode. Among various candidates, TEGDME was selected for its high-performing properties (Fig. 3a and Supplementary Fig. 8). First, TEGDME demonstrates high stability against $*CO_2^{2-}$, as proved by FTIR and EIS analyses. FTIR spectra reveal that no

side products (HCO$_2$Li/CH$_3$CO$_2$Li) were detected during the discharge-charge cycle in the bare TEGDME cell (Supplementary Fig. 9). EIS spectra further confirm high stability of TEGDME at interface, showing that the increased impedance after discharge returned to its original value after recharge (Supplementary Fig. 10). Second, TEGDME exhibits strong coordination ability with Li$^+$ ions, as indicated by the largest disparity between the absolute values of the lowest ESP ($|ESP_{min}|$) and the highest ESP ($|ESP_{max}|$) (Fig. 3b) and further supported by comparative data in Supplementary Fig. 11. For a solvating solvent, $|ESP_{min}|$ should be higher than ESP_{max}, ($|ESP_{min}| > ESP_{max}$), and a larger difference between these values corresponds to stronger coordination strength with cations[22,36,37]. Thus, in the decoupled TEGDME/DMF electrolyte, TEGDME preferentially enters the Li$^+$ solvation shell over DMF. Furthermore, Li$^+$ ions solvated with TEGDME display more positive ESP values compared to those solvated with DMF, as shown in the calculated ESP maps in Supplementary Fig. 12, promoting the preferential adsorption of TEGDME on the positive electrode during discharge. Additionally, [CO$_2$:TEGDME] shows a higher interaction energy (−0.137 eV) compared to [CO$_2$:DMF] (−0.125 eV) (Supplementary Fig. 13), enhancing CO$_2$ solubility in the decoupled electrolyte and enabling CO$_2$ to interact with TEGDME rather than DMF[38]. These features of the decoupled electrolyte create an inert, TEGDME-rich

Fig. 2 | DMF-based electrolytes with enhanced battery kinetics and interfacial instability in Li-CO₂ batteries. All electrolytes contain 1 M LiFSI salt, all the tests were performed at room temperature. **a** Viscosity of TEGDME, DMSO, and DMF solvents. **b** Ionic conductivity of various electrolytes (1 M LiFSI/solvent). **c** Structures and binding energies of Li⁺-TEGDME, Li⁺-DMSO, and Li⁺-DMF. Color scheme of molecules: Li, green; C, light blue; O, red; S, yellow; N, navy; H, white. **d** Long-term voltage-time profiles at 0.1 A g⁻¹ with a cut-off specific capacity of 500 mA h g⁻¹. Two insets show the cycling profiles of the DMF cell during the first 10 cycles and the last 4 cycles, respectively. The DMF cell suddenly failed at the 73rd cycle. **e** Comparison of battery overpotential based on the cycling performance. **f** Rate performance at various current densities from 0.1 to 2 A g⁻¹. **g** Ex-situ FTIR spectra observed on the fresh positive electrode before cycling and the positive electrode discharged and recharged in the DMF cell. The discharge product Li₂CO₃ is marked by blue shading. The side products (HCO₂Li/CH₃CO₂Li), marked with red asterisk (*), result from the irreversible side reaction between DMF and the intermediate CO₂²⁻ radicals during discharge. The detailed reaction mechanism is illustrated in figure **h**. **h** The mechanism for side reactions between DMF and CO₂²⁻ during discharge[19].
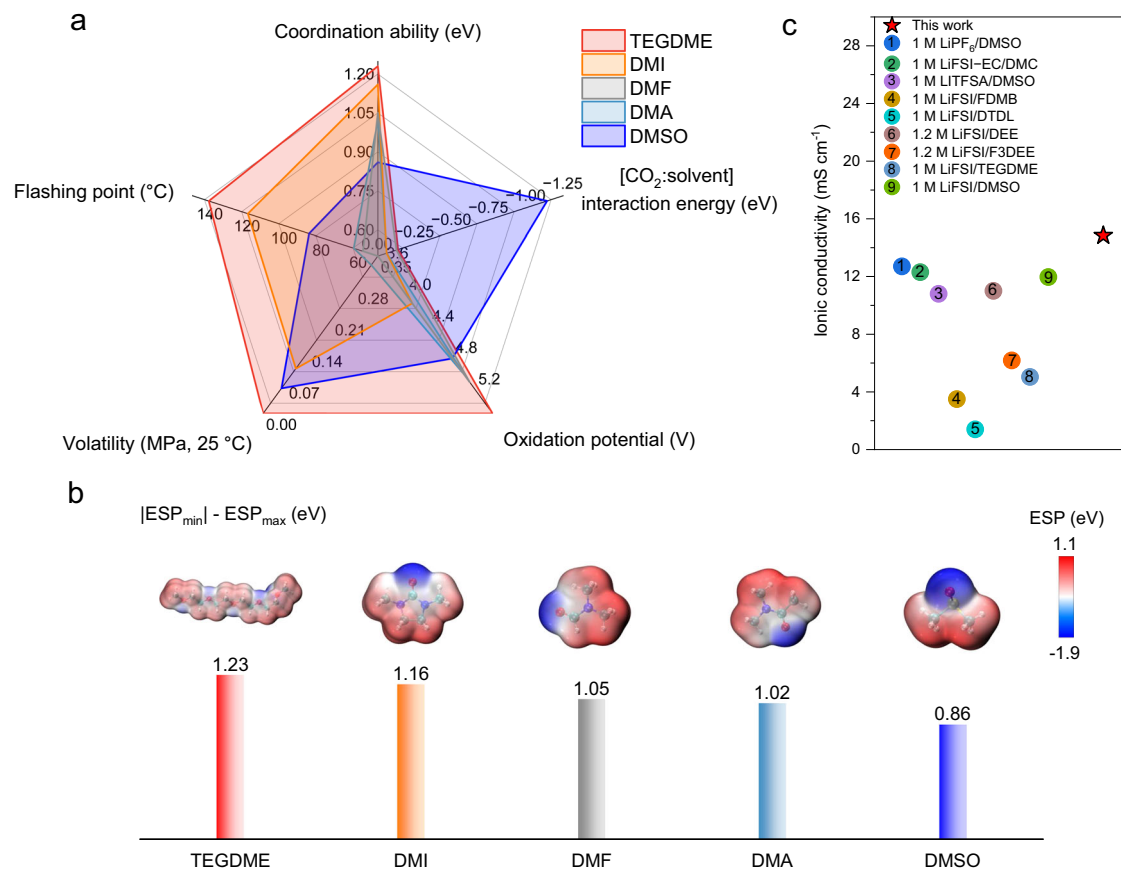
localized environment on the positive electrode, effectively suppressing DMF-related side reactions. More importantly, at low TEGDME concentrations (volume ratio <30%, molar ratio <13%), the decoupled electrolytes can maintain high ionic conductivity, outperforming most reported battery electrolytes (Fig. 3c and Supplementary Table 2)[7,39–43].

Local environment near the positive electrode during discharge
It is found that introducing TEGDME into DMF-based electrolytes reduces the participation of DMF in the Li⁺ solvation shells. As shown in Supplementary Fig. 14, both ¹H and ¹³C NMR spectra exhibit pronounced downfield shifts of the peaks corresponding to DMF in the 3G7F electrolyte compared to those in the bare DMF electrolyte. These shifts suggest reduced electron density around DMF molecules, which is attributed to the weakened interaction between DMF and Li⁺[44,45]. To further investigate the differences in solvation structures between bare DMF electrolyte and decoupled electrolyte, Raman spectra analyses and MD simulations were conducted. Raman spectra (Supplementary Fig. 15) reveal that as the volume ratio of TEGDME increases up to 30% (denoted as 3G7F), the O=C−N bending vibration of

solvated DMF at 675.9 cm⁻¹ is significantly weakened, while the characteristic peaks of TEGDME become more pronounced compared to those at lower TEGDME concentrations (10% and 20%)[46]. This change in solvation structures has a positive effect on battery performance, as demonstrated by the discharge-charge profiles of Li-CO₂ cells, in which the cell employing the 3G7F electrolyte delivered stable, flat discharge/charge plateaus and a low overpotential of ~1 V (Supplementary Fig. 16). Furthermore, radial distribution function (RDF) calculations show that in the 3G7F electrolyte, the peak of Li-O (TEGDME) bond presents a higher intensity and a shorter distance (2.02 Å) compared to that (2.06 Å) of Li-O (DMF) bond, as shown in Supplementary Fig. 17. Specifically, the coordination number of DMF decreases from 2.2 in the bare DMF electrolyte to 1.4 in the 3G7F electrolyte (Supplementary Fig. 18).

Along with the reduced participation of DMF in Li⁺ solvation shells, TEGDME integrates into the Li⁺ solvation shells, rendering solvated Li⁺ ions relatively positive ESP values. To confirm this, MD simulations were conducted to analyse and compare the solvation structures, distribution, and ESP values of Li⁺ ions in the bare DMF and

Fig. 3 | Decoupled electrolyte design. a Radar plot evaluating the key properties of co-solvent candidates, including coordination ability with cations ($|ESP_{min}|-ESP_{max}$, eV), CO_2 solubility (the interaction energies for CO_2:solvent complexes, eV), oxidation potential (Ar), volatility, and flashing point. The detailed values are provided in Supplementary Table 1. b Comparison of the $|ESP_{min}|-ESP_{max}$ value for DMF and co-solvent candidates, including TEGDME, DMI, DMA, and DMSO. The carbon, oxygen, nitrogen, sulphur, and hydrogen atoms are marked as light blue, red, navy, yellow, and white, respectively. c Comparison of ionic conductivity of the decoupled electrolyte and previously reported battery electrolytes. The decoupled electrolyte, composed of TEGDME and DMF in volume ratios of 3:7, exhibits higher ionic conductivity compared to the others. The detailed values are provided in Supplementary Table 2.
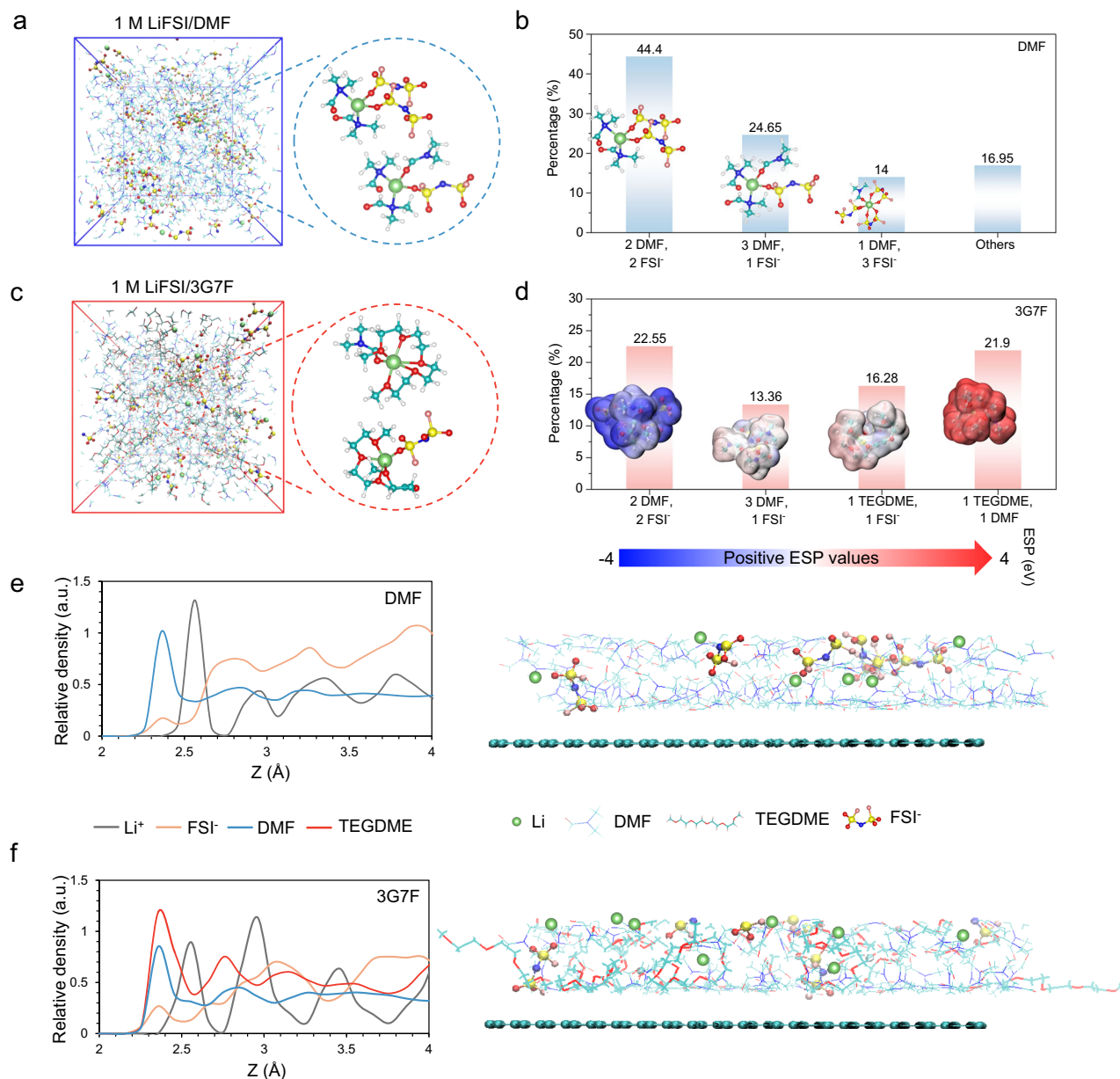
3G7F electrolytes (Supplementary Table 3). In the bare DMF electrolyte, all Li^+ solvation structures contain DMF (Fig. 4a, b). During discharge, MD simulations show that DMF molecules accumulate near the positive electrode (Supplementary Fig. 19), as revealed by accumulated density profiles (Fig. 4e). This localized environment renders DMF molecules vulnerable to attack by $*CO_2^{2-}$, leading to its decomposition and the formation of side products (HCO_2Li/CH_3CO_2Li). With the addition of TEGDME, there are newly-emerged solvation structures of Li[FSI][TEGDME] (16.3%) and Li[DMF][TEGDME] (21.9%) in the 3G7F electrolyte (Fig. 4c). These structures exhibit more positive ESP values compared to those solvated with DMF (Fig. 4d and Supplementary Fig. 20), resulting in a larger electric potential difference between the negatively charged positive electrode (during discharge) and these solvated Li^+ ions. Consequently, the positive electrode preferentially attracts Li^+ ions solvated with TEGDME, thus enriching TEGDME near the positive electrode surface and creating a TEGDME-rich and DMF-poor localized environment. As evidenced by the MD simulations (Supplementary Fig. 21) and the accumulated density profiles (Fig. 4f), the density of TEGDME molecules near the positive electrode surface is higher than that of DMF in the 3G7F electrolyte. Furthermore, TEGDME after desolvation has a higher LUMO energy value (−0.53 eV, Supplementary Fig. 22 and Table 4) than DMF (−0.73 eV), indicating TEGDME is more stable than DMF. Meanwhile, the highly conductive DMF remains in the bulk electrolyte, ensuring high ionic conductivity of the 3G7F electrolyte, which surpasses that of most reported battery electrolytes (Fig. 3c). By designing such a decoupled electrolyte, DMF-

related side reactions on the positive electrode surface can be effectively suppressed while maintaining fast ion transport in the bulk electrolyte, ultimately improving battery performance.

Enhanced battery performance via a decoupled electrolyte
Li-CO_2 cells using the decoupled electrolyte demonstrated enhanced electrochemical stability. Notably, the cell employing the 3G7F decoupled electrolyte (denoted as 3G7F cell) achieved a significantly prolonged cycle life of ~2600 h, a stable charge plateau at ~3.8 V, and a low overpotential close to 1 V with a metal-free rGO catalyst (Fig. 5a). This electrochemical performance surpasses most recently reported Li-CO_2 batteries with metal-free catalysts (Fig. 5b and Supplementary Table 5)[47–53]. The improved stability was further validated by its rate performance. As shown in Fig. 5c, the 3G7F cell consistently demonstrated lower over-potentials and stable discharge/charge plateaus across current densities from 0.1 to 2 A g⁻¹, outperforming the bare DMF cell. Moreover, the 3G7F cell exhibited a marked improvement in full-discharge capacity, delivering 16,781, 13,893, 11,578, and 9379 mAh g⁻¹ at 0.2, 0.4, 0.5, and 1 A g⁻¹, respectively (Supplementary Fig. 24)−approximately double those of the bare DMF cell, which achieved 4008, 6662, 7835, and 8682 mAh g⁻¹ at 0.2, 0.4, 0.5, and 1 A g⁻¹, respectively (Supplementary Fig. 25).

To confirm the suppression of DMF-related side reactions in the 3G7F cell, in-situ differential electrochemical mass spectrometry (DEMS) was employed to monitor the real-time consumption and
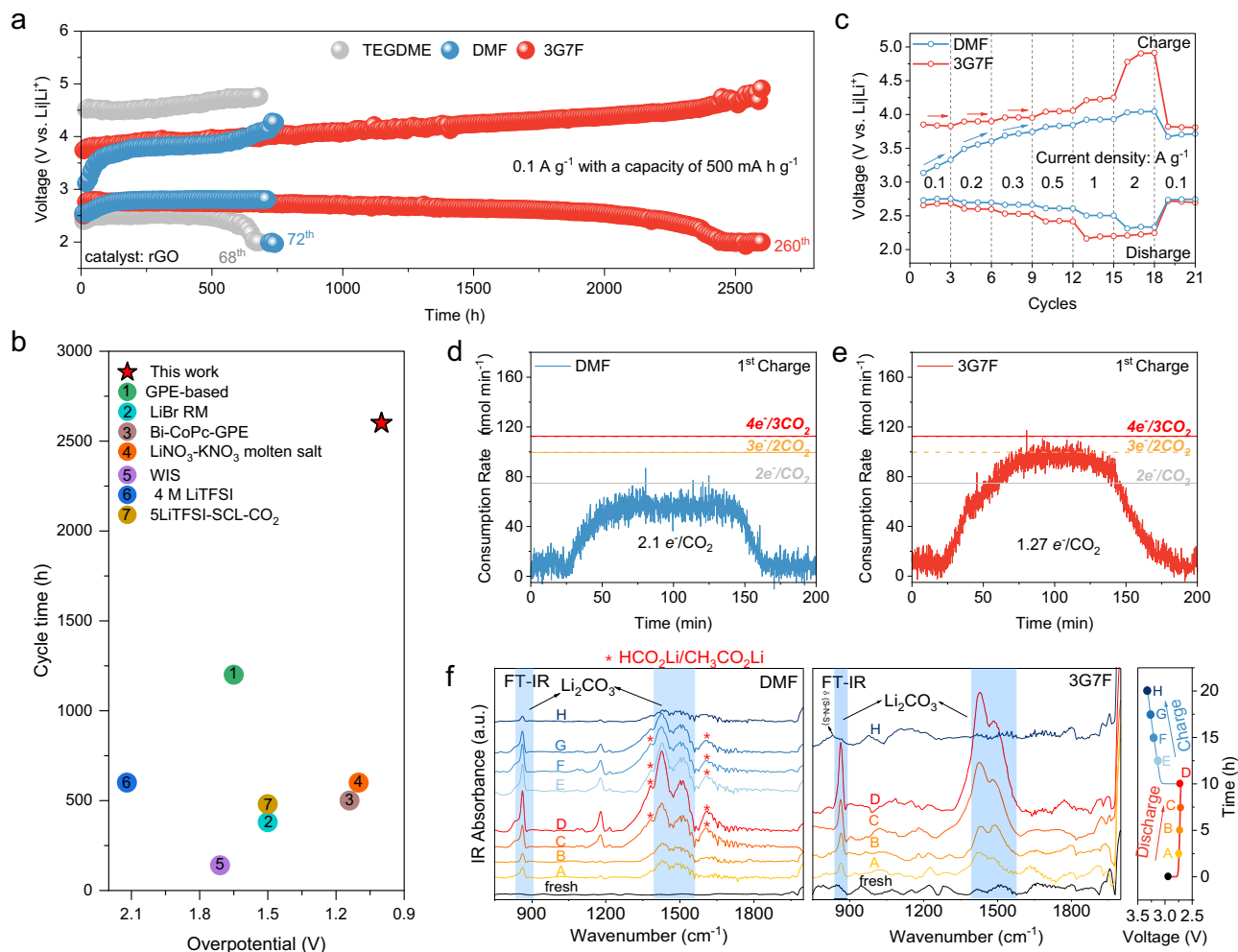
Fig. 4 | Solvation structures and localized environment near the positive electrode during discharge in the bare DMF electrolyte and 3G7F decoupled electrolyte. Snapshots and typical Li$^+$ clusters of the **a** bare DMF and **c** 3G7F electrolytes obtained from MD simulations. Distribution of possible solvation structures, structures of the most probable inner solvation shells of Li$^+$ ions for the **b** bare DMF and **d** 3G7F electrolytes, obtained by MD simulations. The structures of the Li$^+$ solvation cluster are provided in Supplementary Data 1. In the 3G7F electrolyte, Li$^+$ clusters solvated with TEGDME demonstrate relatively more positive ESP maps. Interfacial cumulated density profiles of Li$^+$, FSI$^-$, and solvent molecules (DMF and TEGDME) and schematic snapshots (side view) of the localized environment near the positive electrode during discharge in the **e** bare DMF and **f** 3G7F electrolytes, respectively. Z: distance from the positive electrode surface. Density: the ratio of the number of molecules to that near neutrally charged positive electrodes (Supplementary Fig. 23). Color scheme of molecules: Li, green; C, light blue; O, red; S, yellow; N, navy; H, white; F, pink.

evolution of CO_2, as well as the related charge-to-mass ratio. During the discharge process, CO_2 was consumed (Supplementary Fig. 26), while its evolution was observed during the charge process. For the bare DMF cell (Fig. 5d), the charge-to-mass ratio of CO_2 (e^-/CO_2) during charge was determined to be 2.1, which largely exceeds the theoretical value of $4e^-/3CO_2$ (1.33) corresponding to the reaction of $2Li_2CO_3 + C \leftrightarrow 3CO_2 + 4Li^+ + 4e^-$[29,52]. This suggests the involvement of the decomposition of side products during charge, consistent with observations in the previous section. In contrast, the e^-/CO_2 for the 3G7F cell is 1.27 (Fig. 5e), which is very close to the theoretical value of 1.33 ($4e^-/3CO_2$). This provides direct evidence that the charge mechanism in the 3G7F cell mainly involves the decomposition of

reversible Li_2CO_3, highlighting its enhanced electrolyte stability and the effective suppression of side reactions.

Ex-situ FTIR spectra collected at different discharge/charge states verified the inhibition of side reactions between DMF and CO_2^{2-} in the 3G7F cell. As shown in Fig. 5f, the bare DMF cell showed prominent signals of side products, corresponding to HCO_2Li/CH_3CO_2Li, during discharging[35,53]. While these side products gradually disappeared during charging, residual Li_2CO_3 remained even after the cell was fully charged. This suggests that the charge process involved the decomposition of side products, consistent with the in-situ DEMS results (Fig. 5d, e). In contrast, no signal of side products was observed in the 3G7F cell, accompanied by no Li_2CO_3 residual at the end of charging.

Fig. 5 | Enhanced electrochemical stability via the decoupled electrolyte.
a Long-term cycling performance of the bare TEGDME, bare DMF, and 3G7F cells at
0.1 A g^{-1} with a cut-off specific capacity of 500 mA h g^{-1}. **b** Comparison of over-
potential and cycle life with previously reported electrolytes optimized for Li-CO$_2$
batteries with a metal-free catalyst. The detailed values are provided in Supple-
mentary Table 5. **c** Rate performance of the bare DMF and 3G7F cells at various
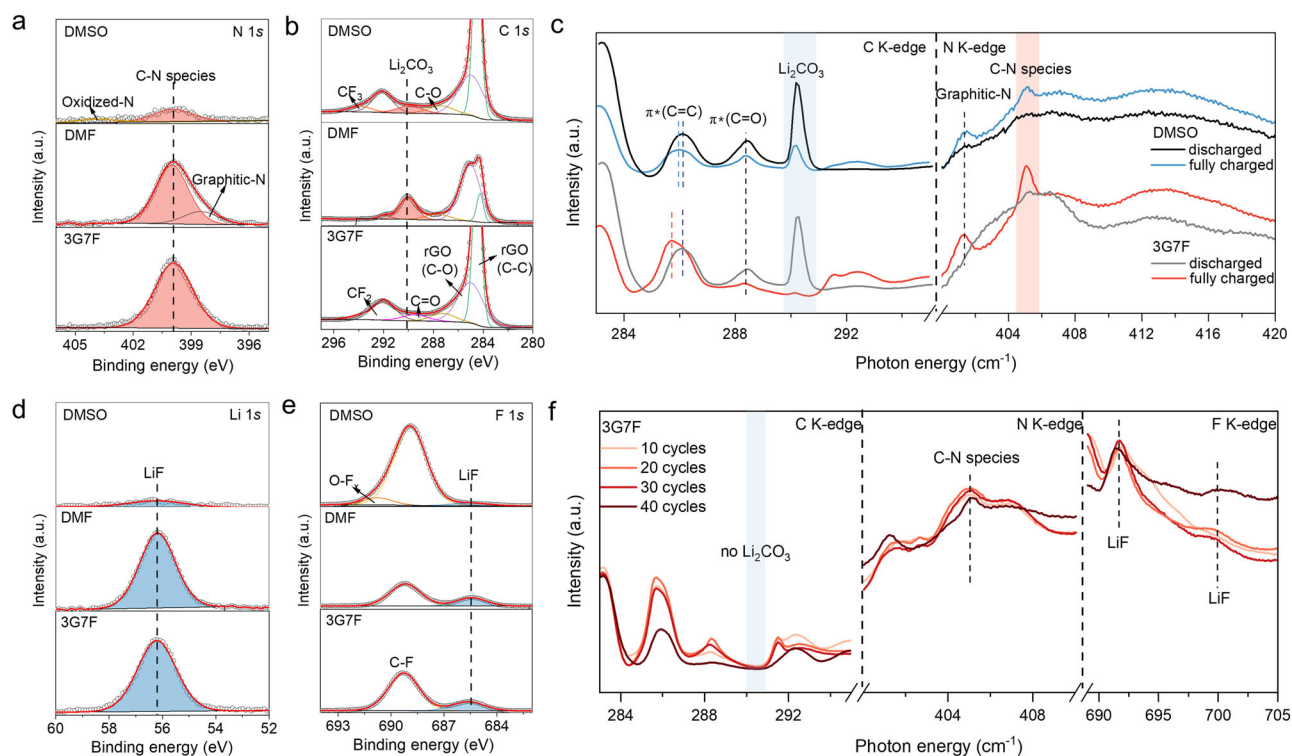current densities from 0.1 to 2 A g^{-1}. In-situ DEMS results for the **d** bare DMF and
e 3G7F cells during the first charge, tested at 200 μA within a capacity of 400 μAh.
f Ex-situ FTIR spectra observed on positive electrode surfaces during the first cycle
at 0.1 A g^{-1} and collected at different discharge/charge states. The discharge pro-
ducts (Li$_2$CO$_3$) are highlighted with blue shading. The side products (HCO$_2$Li/
CH$_3$CO$_2$Li) are marked with red * symbol.

Photographs of separators and lithium negative electrodes after
cycling further proved the high stability of the 3G7F cell (Supple-
mentary Fig. 27). After 10 cycles, the separator in the bare DMF cell
turned brown and adhered tightly to the lithium negative electrode,
indicating severe electrolyte decomposition. By contrast, the separa-
tor and lithium negative electrode in the 3G7F cell displayed almost no
color change or damage. These in-situ and ex-situ observations cross-
validate that the 3G7F decoupled electrolyte can effectively suppress
DMF-related side reactions, thus achieving enhanced electrochemical
cycling stability.

SEI analysis and the reversibility of Li$_2$CO$_3$
It is widely known that the high charging potential and large polar-
ization in Li-CO$_2$ batteries are mainly caused by the sluggish oxida-
tion kinetics of the discharge product Li$_2$CO$_3$ at the electrolyte|
positive electrode interface[54,55]. With the same catalyst (rGO), the
improved CO$_2$ reaction kinetics and reduced overpotential observed
in DMF-based electrolytes compared to others may be attributed to
the catalytic effects of SEI compositions towards Li$_2$CO$_3$ decom-
position. As explored in our previous work[31], in-situ formed C-N
species in SEI layers provide strong adsorption sites for CO$_2$, *CO$_2^{2-}$,
and Li$_2$CO$_3$, facilitating charge transfer from C-N species at the

interface to *CO$_2^{2-}$ during discharge and from Li$_2$CO$_3$ to the interfacial
N sites of C-N species during charge, thereby building a bidirectional
fast-reacting bridge for CRR/CER kinetics and effectively alleviating
the accumulation of Li$_2$CO$_3$ residuals. Thus, XPS was employed to
analyse the chemical compositions of SEI layers formed on the cycled
positive electrodes in the 3G7F cell (after 5 cycles, Supplementary
Fig. 28). To evaluate the effect of C-N species content on enhancing
the reversibility of Li$_2$CO$_3$ and reducing overpotential, the positive
electrodes cycled in the DMSO and bare DMF cells were used for
comparison. In the N 1s XPS spectra (Fig. 6a), the peak corresponding
to C-N species at 399.9 eV exhibited significantly higher intensity in
both the bare DMF and 3G7F cells[31,56,57], due to the catalytic effect of
C-N species in facilitating CRR and CER reactions, thus contributing
to the reduced overpotential (-1 V). In contrast, only a small peak
associated with C-N species can be observed for the DMSO cell,
correspondingly, the DMSO cell delivered a relatively larger polar-
ization (1.62 V). Meanwhile, the C 1s XPS spectra (Fig. 6b) reveal that
the 3G7F cell, with a higher content of C-N species, enabled the
complete decomposition of Li$_2$CO$_3$, unlike the DMSO cell, which
remained a large amount of Li$_2$CO$_3$ residuals[32]. These observations
confirm the critical role of C-N species in promoting Li$_2$CO$_3$ decom-
position and governing battery reaction kinetics. The positive

Fig. 6 | Characterization of the SEI composition on positive electrodes cycled in Li-CO₂ batteries. a N 1s, b C 1s, d Li 1s, and e F 1s XPS spectra for the positive electrodes after 5 cycles (fully charged state) in the cells using the bare DMSO, bare DMF, and 3G7F electrolytes. Notably, Li₂CO₃ residuals in the bare DMF electrolyte (Fig. 6b) was caused by side products (HCO₂Li/CH₃CO₂Li) that decompose at lower charging voltage, as discussed in previous sections. c C K-edge and N K-edge XANES spectra for the positive electrodes discharged and after 5 cycles (fully charged state) in the DMSO and 3G7F cells, respectively. (with the peaks at 285.4, 288.6, and 291.7 eV corresponding to π*(C = C), π*(C = O), and σ*(C = C), respectively). The discharge products (Li₂CO₃) and C-N species are indicated by blue and red shading, respectively. f C K-edge, N K-edge, and F K-edge XANES spectra for the positive electrodes after prolonged cycling (10, 20, 30, and 40 cycles, fully charged state) in the 3G7F cell. (The intense peak at 692 eV and a small post peak at 700 eV are assigned to LiF). The discharge products (Li₂CO₃) is indicated by blue shading.

correlation between C-N species and the reversibility of Li₂CO₃ was further proved by X-ray absorption near-edge spectroscopy (XANES). After 5 cycles (Fig. 6c), the 3G7F cell exhibited no Li₂CO₃ residuals, consistent with a stronger peak of C-N species[31,58], indicating favourable reversibility of Li₂CO₃, reduced battery overpotential, and improved cycling performance. In contrast, the DMSO cell showed a distinct peak of Li₂CO₃ residuals and a low content of C-N species, leading to sluggish battery kinetics[59].

In addition to C-N species, the most distinguishing difference between the DMSO cell and DMF-based cells (bare DMF and 3G7F) lies in the content of FSI−derived SEI components. The peaks at 56.2 eV in the Li 1s spectra (Fig. 6d) and 685.5 eV in the F 1s spectra (Fig. 6e), assigned to LiF, present significantly stronger intensities in the DMF-based cells compared to the DMSO cell[60]. This suggests that the SEI layers formed in the DMF-based cells contain more LiF, indicating that the SEI layers are primarily formed through anion-induced decomposition, as FSI⁻ is the only fluorine source. Additionally, other inorganic species, such as Li₂SO₄ and Li₂SO₃, also show higher contents in the DMF-based cells (Supplementary Fig. 29)[5]. It is well-known that inorganic SEI components, such as LiF, possess high ionic conductivity and mechanical strength[61–64]. These properties not only enhance Li⁺ transport at the interface but also prevent the dissolution of organic C−N species into the electrolyte, thereby preserving the structural integrity of the SEI during cycling. As a result, the persistence of C-N species is ensured, minimizing continuous electrolyte consumption and improving long-term interfacial stability. As evidenced by the XANES spectra (Fig. 6f), there was almost no change in the peak intensity of C-N species and LiF with cycling in the 3G7F cell[65,66]. Moreover, no Li₂CO₃ residuals were detected even after 40 cycles, indicating that organic C-N species remained stable

throughout prolonged discharge/charge processes under the protective effect of LiF. Consequently, C-N species can constantly contribute to promoting Li₂CO₃ decomposition and enhancing battery reaction kinetics. The enhanced reversibility of Li₂CO₃ in the 3G7F cell is further validated by Raman spectra (Supplementary Fig. 30). The Li₂CO₃ peak was clearly observed upon discharge and completely disappeared after recharge, reflecting no Li₂CO₃ residuals even after 40 cycles.

Discussion

Despite its low viscosity, high conductivity, and fast desolvation, DMF alone is unsuitable for Li-CO₂ batteries due to its instability against *CO₂²⁻ at the electrolyte|positive electrode interface. In this work, we developed a decoupled electrolyte (TEGDME/DMF, 3G7F) that combines highly conductive bulk properties of DMF with an inert, TEGDME-rich localized environment near the positive electrode to suppress DMF-related side reactions. Theoretical calculations reveal that during discharge, Li⁺ ions solvated with TEGDME exhibit relatively positive ESP values compared to those solvated with DMF, which favors preferential adsorption of TEGDME on the positive electrode. This creates a TEGDME-rich, inert localized environment that effectively inhibits side reactions between DMF and *CO₂²⁻, enhancing the interfacial stability. Meanwhile, highly conductive DMF remains in the bulk electrolyte to ensure favourable battery kinetics. With this decoupled electrolyte, Li-CO₂ cells achieved high reversibility of Li₂CO₃ and improved battery performance, enabling a long cycle life of ~2600 h, a low charge plateau of 3.8 V, and a small overpotential of 1 V. Such a decoupled electrolyte design could be extended to other battery systems, such as metal-air batteries. Additionally, the simple preparation process of the

electrolyte makes it suitable for large-scale production. Our work opens an alternative avenue for electrolyte design beyond conventional SEI construction and may trigger interest in previously underexplored solvents for next-generation batteries.

Methods

Preparation of electrolytes

All electrolytes were prepared and stored in a 10 mL glass vial in an argon-filled glove box (O_2 and H_2O levels below 0.1 ppm) at room temperature (25 °C) before cell assembly. Electrolytes were transferred using polypropylene (PP) pipette tips. In this work, lithium bis(fluorosulfonyl)imide (LiFSI, 99.5%, Canrd) was dried under vacuum at 80 °C overnight. Solvents, including N,N-dimethylformamide (DMF, 99.9%, Sigma-Aldrich), DMSO (99.9%, Sigma-Aldrich), N,N-dimethylacetamide (DMA, 99.9%, Sigma-Aldrich), 1,3-dimethyl-2-imidazolidinone (DMI, 99.5%, Sigma-Aldrich), and TEGDME (99%, Sigma-Aldrich), were dried twice with freshly activated 4 Å molecular sieves. The concentration for electrolytes are expressed as moles of salt/volume of solvents, for example, 1 M LiFSI/DMF refers to 1 mol LiFSI dissolved in 1 L DMF solvent. The decoupled electrolytes were prepared by dissolving 1 M LiFSI in a mixture of TEGDME and DMF with volume ratios of 1:9, 2:8, 3:7, 4:6, and 5:5, respectively. The molar ratios of TEGDME in these electrolytes are approximately 3.8%, 8%, 13%, 20%, and 26%.

Preparation of electrodes

The negative electrodes were circular lithium chips (Canrd, China) with a purity of 99.95%. The lithium chips were pre-cut into circular disks with a diameter of 16 mm and a thickness of 0.6 mm. The lithium electrodes were stored and handled in an Ar-filled glovebox (O_2 and H_2O levels below 0.1 ppm) to prevent surface oxidation. No additional chemical treatment was applied. The air positive electrodes were prepared via a filtration process. To better explore the key role of solvents in determining the CO_2 reaction kinetics, commercial rGO with poor catalytic performance was employed as a metal-free catalyst. Typically, 5 mg of rGO and 50 μL of Nafion solution (~5 wt%, Sigma-Aldrich) were dispersed in 2 mL of ethanol, after being ultrasonicated for around 60 min to mix them thoroughly at room temperature (25 °C). After that, the suspension was filtered on a piece of Toray carbon paper (TGP-H-060), which was punched out into circular sheets with a diameter of 9.5 mm. After being dried at 70 °C overnight, the catalysts were uniformly coated on the Toray carbon paper. Each positive electrode contains a rGO loading of 0.2 mg. Here, the catalyst-loaded Toray carbon paper discs served as air positive electrodes in the Li-CO_2 cells.

Electrochemical measurements

For electrochemical tests, CR2032-type coin cells (16 holes on the positive electrode side) were assembled in an Ar-filled glove box with the air positive electrodes and lithium negative electrodes separated by glass fiber separators (Grade 363, Filtech, Australia; CAT NO: 0363-240/25). The separator has an average particle retention capability of approximately 1.0 μm and a thickness of ~0.66 mm. Circular separators with a diameter of 240 mm were received from the supplier and stored in a dry environment prior to use. Before cell assembly, the separators were manually cut into circular disks with a diameter of 19 mm using a punch. No drying process was required due to the anhydrous nature of the packaging and storage conditions. The separators were symmetric and thus applied without orientation preference between the positive and negative electrodes. Solutions of 1 M single-solvent and dual-solvent electrolytes were used. During cell assembly, 90 μL of the electrolyte was added using PP pipette tips. The electrolyte was evenly distributed and allowed to fully wet the separator prior to sealing. The as-prepared coin cells were sealed in CO_2-filled bottles for Li-CO_2 battery tests. All electrochemical measurements were carried out in a temperature-controlled battery testing room maintained at 25 °C. The galvanostatic discharge/charge tests were carried out in the cut-off voltage range of 2–4.5 V at different current densities (from 0.1 to 2 A g^{-1}) using a battery test station (Land, China). Linear sweep voltammetry (LSV) was conducted on each cell from the open-circuit voltage (Voc) to 6 V (vs. Li|Li$^+$) with a scan rate of 1 mV s^{-1}. EIS was performed over the frequency range of 100 kHz to 10 MHz with a perturbation amplitude of ±10 mV using a VMP3 potentiostat/galvanostat (BioLogic). Graphing was performed using OriginPro, and data analysis was carried out using the ZSimpWin software. For each electrolyte, five independent coin cells were assembled and tested under identical conditions to ensure reproducibility. The electrochemical data shown in the main figures correspond to the highest-performing cell in each group, selected to demonstrate the full performance potential of the electrolyte under optimized conditions. This approach is commonly adopted in preliminary proof-of-concept studies to highlight the effectiveness of electrolyte engineering.

Ex-situ characterization methods

The ionic conductivity of electrolytes was obtained from a conductivity measurement instrument (DDB-303A, Shanghai INESA & Scientific Instrument Co. Ltd.). ^{13}C and ^{1}H NMR spectroscopy was conducted on the electrolytes to analyse the coordination ability of solvents; additionally, ^{1}H NMR was performed to identify the discharge products on positive electrodes. Before doing the ^{1}H NMR test, the positive electrodes were washed with D_2O, and then the resulting solution was examined. All electrolytes were prepared and sealed in glass vials within an Ar-filled glovebox (H_2O < 0.1 ppm, O_2 < 0.1 ppm). For ex-situ characterization, the samples were stored in the glovebox and were not exposed to air prior to measurement. For characterizing the positive electrodes cycled in Li-CO_2 cells, the cells were disassembled inside an Ar-filled glove box, and the obtained electrodes were thoroughly washed with purified dimethyl carbonate (DMC) to remove salt residues before ex-situ characterization. Field-emission scanning electron microscopy (FESEM, FEI QUANTA 450 FEG with an Oxford Ultim Max Large Area SDD energy-dispersive spectral (EDS) detector) was employed to observe the morphology of the positive electrodes. High-resolution scanning transmission electron microscopy (STEM) images were obtained using a Thermo Scientific Glacios microscope with an accelerating voltage of 200 kV (Cryo-TEM FEI Glacios 200 kV Cryo-Transmission Electron Microscope). XPS was used to detect the chemical compositions on the positive electrode surface on a VG Multilab 2000 (VG) photoelectron spectrometer using monochromatic Al Kα radiation under vacuum of 2×10^{-6} Pa. To avoid air exposure, the Li-CO_2 cells were disassembled in an Ar-filled glove box, and then the cycled positive electrodes were directly transferred to the XPS instrument connected with the argon-filled glove box for testing. The attenuated total reflection−Fourier transform infrared (ATR-FTIR) spectra of the positive electrodes were collected using an offline Hyperion 3000 microscope attached to a Bruker VERTEX V70 spectrometer (using traditional globar source IR). XANES was carried out at the soft X-ray beamline, Australian Synchrotron. The data were processed using Igor Pro 8, with the aid of QANT.

In-situ characterization method

In-situ DEMS was conducted to monitor the consumption and evolution of CO_2 during battery operation on a QAS100 Li (Linglu Instruments (Shanghai) Co., Ltd.) with an electron impact ionization source (EI, 70 eV), argon as the carrier gas (1 mL/min) and a secondary electron multiplier (SEM) detector (1100 V). The batteries were tested at a constant current of 200 μA within a capacity of 400 μAh.

Theoretical calculations

The simulation systems used the following ratios for each component:

System	Number of components		
	Li$^+$	FSI$^-$	Solvent
1 M LiFSI/DMF	1	1	DMF = 13
1 M LiFSI in 30% TEGDME and 70% DMF	10	10	TEGDME = 16.6, DMF = 98

All molecular dynamics (MD) simulations were conducted using the GROMACS package with the Optimized Potentials for Liquid Simulations force field. Force field topologies was generated via ACPYPE. Bulk electrolyte systems were modeled in cubic boxes (5 × 5 × 5 nm^3) containing Li salts and solvents. Short-range van der Waals and Coulombic interactions were truncated at 1.2 nm, while long-range electrostatics were calculated using the particle-mesh Ewald approach (Fourier grid spacing of 0.12 nm). The LINCS algorithm was applied to constrain bond vibrations, and periodic boundary conditions were enforced in all three directions. Each system underwent initial energy minimization, followed by equilibration runs of 1 ns in the NVT ensemble and 1 ns in the NPT ensemble with a 1 fs integration step. Production trajectories were collected over 30 ns at 298 K under the Nosé-Hoover thermostat with a relaxation time of 1 ps. Structural and dynamic properties such as mean square displacement and diffusion coefficients were extracted using built-in GROMACS utilities.

The analysis of MD trajectories (i.e., mean square displacement and diffusion coefficient) was performed using standard tools within GROMACS. DFT calculations were used to investigate several Li solvation structures observed from the MD simulations. Geometry optimizations and electronic structure calculations were performed using the Vienna Ab initio Simulation Package with the projector-augmented wave method and the Perdew–Burke–Ernzerhof functional. A plane-wave energy cut-off of 500 eV and a single Gamma k-point sampling were employed to evaluate the molecular orbital energies (i.e., lowest unoccupied molecule orbital (LUMO) and highest occupied molecular orbital) and interactions between different species in solution. Gaussian was used to obtain the ESP of Li solvation structures. In this work, the solvation structures were taken from the MD simulations and underwent further DFT geometry optimization before the ESP calculations were performed. DFT calculations were conducted using Gaussian with B3LYP (Becke, 3-parameter, Lee-Yang-Parr) functional with 6–31 G(d,p) basis set. And the geometry optimization was performed prior to the ESP mapping. The initial and final configurations from MD simulations are shown in Supplementary Data 2.

Data availability

Source data are provided with this paper. All other data are available from the authors upon request. Source data are provided with this paper.

References

1. Winter, M., Barnett, B. & Xu, K. Before Li ion batteries. *Chem. Rev.* **118**, 11433–11456 (2018).
2. Xu, K. Nonaqueous liquid electrolytes for lithium-based rechargeable batteries. *Chem. Rev.* **104**, 4303–4418 (2004).
3. Hao, B. et al. Concentration polarization induced phase rigidification in ultralow salt colloid chemistry to stabilize cryogenic Zn batteries. *Nat. Commun.* **15**, 9465 (2024).
4. Meng, Y. S., Srinivasan, V. & Xu, K. Designing better electrolytes. *Science* **378**, eabq3750 (2022).
5. Zhang, W. et al. Regulating the reduction reaction pathways via manipulating the solvation shell and donor number of the solvent in Li–CO$_2$ chemistry. *Proc. Natl. Acad. Sci. USA* **120**, 2219692120 (2023).
6. Zhang, F., Zhang, W., Wexler, D. & Guo, Z. Recent progress and future advances on aqueous monovalent-ion batteries towards safe and high-power energy storage. *Adv. Mater.* **34**, 2107965 (2022).
7. Yu, Z. et al. Rational solvent molecule tuning for high-performance lithium metal battery electrolytes. *Nat. Energy* **7**, 94–106 (2022).
8. Han, B. et al. Probing the Na metal solid electrolyte interphase via cryo-transmission electron microscopy. *Nat. Commun.* **12**, 3066 (2021).
9. Zhao, Y., Zhou, T., Mensi, M., Choi, J. W. & Coskun, A. Electrolyte engineering via ether solvent fluorination for developing stable non-aqueous lithium metal batteries. *Nat. Commun.* **14**, 299 (2023).
10. Von Aspern, N., Röschenthaler, G. V., Winter, M. & Cekic-Laskovic, I. Fluorine and lithium: ideal partners for high-performance rechargeable battery electrolytes. *Angew. Chem. Int. Ed.* **58**, 15978–16000 (2019).
11. Wang, Y. et al. Emerging electrolytes with fluorinated solvents for rechargeable lithium-based batteries. *Chem. Soc. Rev.* **52**, 2713–2763 (2023).
12. Meng, Y. et al. Robust bilayer solid electrolyte interphase for Zn electrode with high utilization and efficiency. *Nat. Commun.* **15**, 8431 (2024).
13. Cheng, X. B., Zhang, R., Zhao, C. Z. & Zhang, Q. Toward safe lithium metal anode in rechargeable batteries: a review. *Chem. Rev.* **117**, 10403–10473 (2017).
14. Mu, X., Pan, H., He, P. & Zhou, H. Li–CO$_2$ and Na–CO$_2$ batteries: toward greener and sustainable electrical energy storage. *Adv. Mater.* **32**, 1903790 (2020).
15. You, L. et al. N-dimethylformamide electrolyte additive via a blocking strategy enables high-performance lithium-ion battery under high temperature. *J. Phys. Chem. C.* **123**, 5942–5950 (2019).
16. Wang, N. et al. Zinc–organic battery with a wide operation-temperature window from −70 to 150 °C. *Angew. Chem. Int. Ed.* **59**, 14577–14583 (2020).
17. Yuan, X. et al. Low concentration DMF/H$_2$O hybrid electrolyte: a new opportunity for anode materials in aqueous potassium-ion batteries. *ACS Appl. Mater. Interfaces* **13**, 38248–38255 (2021).
18. Kong, S. et al. Anchoring polar organic molecules in defective ammonium vanadate for high-performance flexible aqueous zinc-ion battery. *Small* **19**, 2304462 (2023).
19. Chen, Y., Freunberger, S. A., Peng, Z., Bardé, F. & Bruce, P. G. Li–O$_2$ battery with a dimethylformamide electrolyte. *J. Am. Chem. Soc.* **134**, 7952–7957 (2012).
20. Murray, J. S. & Politzer, P. Molecular electrostatic potentials and noncovalent interactions. *Wiley Interdiscip. Rev. Comput. Mol. Sci.* **7**, e1326 (2017).
21. Wang, Z. et al. Non-flammable ester electrolyte with boosted stability against Li for high-performance Li metal batteries. *Angew. Chem. Int. Ed.* **134**, e202206682 (2022).
22. Wu, Y. et al. Electrostatic potential as solvent descriptor to enable rational electrolyte design for lithium batteries. *Adv. Energy Mater.* **13**, 2300259 (2023).
23. Chen, J. et al. Hybridizing carbonate and ether at molecular scales for high-energy and high-safety lithium metal batteries. *Nat. Commun.* **15**, 3217 (2024).
24. Chu, H. et al. Achieving three-dimensional lithium sulfide growth in lithium-sulfur batteries using high-donor-number anions. *Nat. Commun.* **10**, 188 (2019).
25. Wang, Y. et al. Decreasing the overpotential of aprotic Li-CO$_2$ batteries with the in-plane alloy structure in ultrathin 2D Ru-based nanosheets. *Adv. Funct. Mater.* **32**, 2202737 (2022).
26. Hou, Y. et al. Mo$_2$C/CNT: an efficient catalyst for rechargeable Li–CO$_2$ batteries. *Adv. Funct. Mater.* **27**, 1700564 (2017).

27. Zhang, J. et al. Rechargeable Li-CO$_2$ batteries with graphdiyne as efficient metal-free cathode catalysts. *Adv. Funct. Mater.* **31**, 2101423 (2021).

28. Wang, H. et al. Dual-solvent Li-ion solvation enables high-performance Li-metal batteries. *Adv. Mater.* **33**, 2008619 (2021).

29. Qiao, Y. et al. Li-CO2 electrochemistry: a new strategy for CO$_2$ fixation and energy storage. *Joule* **1**, 359–370 (2017).

30. Jiao, Y. et al. Recent progress and prospects of Li-CO$_2$ batteries: mechanisms, catalysts and electrolytes. *Energy Storage Mater.* **34**, 148–170 (2021).

31. Zhang, F. et al. Catalytic role of in-situ formed C-N species for enhanced Li$_2$CO$_3$ decomposition. *Nat. Commun.* **15**, 3393 (2024).

32. Qiao, Y. et al. 3D-printed graphene oxide framework with thermal shock synthesized nanoparticles for Li-CO$_2$ batteries. *Adv. Funct. Mater.* **28**, 1805899 (2018).

33. Freunberger, S. A. et al. The lithium–oxygen battery with ether-based electrolytes. *Angew. Chem. Int. Ed.* **37**, 8609–8613 (2011).

34. Freunberger, S. A. et al. Reactions in the rechargeable lithium–O$_2$ battery with alkyl carbonate electrolytes. *J. Am. Chem. Soc.* **133**, 8040–8047 (2011).

35. Ottakam Thotiyl, M. M., Freunberger, S. A., Peng, Z. & Bruce, P. G. The carbon electrode in nonaqueous Li–O$_2$ cells. *J. Am. Chem. Soc.* **135**, 494–500 (2013).

36. Rustomji, C. S. et al. Liquefied gas electrolytes for electrochemical energy storage devices. *Science* **356**, eaal4263 (2017).

37. Zhang, G. et al. High-energy and fast-charging lithium metal batteries enabled by tuning Li+-solvation via electron-withdrawing and lithiophobicity functionality. *Nat. Commun.* **16**, 1–12 (2025).

38. Lindberg, J. et al. Li salt anion effect on O$_2$ solubility in an Li–O$_2$ battery. *J. Phys. Chem. C.* **122**, 1913–1920 (2018).

39. Koo, B., Lee, H., Hwang, S. & Lee, H. Ionic conduction and speciation in LiPF6 and LiBF4 dimethyl sulfoxide electrolytes: comparison with propylene carbonate electrolytes. *J. Phys. Chem. C.* **127**, 5676–5682 (2023).

40. Berhaut, C. L. et al. Ionic association analysis of LiTDI, LiFSI and LiPF$_6$ in EC/DMC for better Li-ion battery performances. *RSC Adv.* **9**, 4599–4608 (2019).

41. Galvez-Aranda, D. E. & Seminario, J. M. Ion pairing, clustering and transport in a LiFSI-TMP electrolyte as functions of salt concentration using molecular dynamics simulations. *J. Electrochem. Soc.* **168**, 040511 (2021).

42. Yu, Z. et al. Molecular design for electrolyte solvents enabling energy-dense and long-cycling lithium metal batteries. *Nat. Energy* **5**, 526–533 (2020).

43. Zhao, Y. et al. Fluorinated ether electrolyte with controlled solvation structure for high voltage lithium metal batteries. *Nat. Commun.* **13**, 2575 (2022).

44. Amanchukwu, C. V. et al. A new class of ionically conducting fluorinated ether electrolytes with high electrochemical stability. *J. Am. Chem. Soc.* **142**, 7393–7403 (2020).

45. Chen, Y. et al. Steric effect tuned ion solvation enabling stable cycling of high-voltage lithium metal battery. *J. Am. Chem. Soc.* **143**, 18703–18713 (2021).

46. Fujii, K., Wakamatsu, H., Todorov, Y., Yoshimoto, N. & Morita, M. Structural and electrochemical properties of Li ion solvation complexes in the salt-concentrated electrolytes using an aprotic donor solvent, N, N-dimethylformamide. *J. Phys. Chem. C.* **120**, 17196–17204 (2016).

47. Li, J. et al. Drawing a pencil-trace cathode for a high-performance polymer-based Li–CO$_2$ battery with redox mediator. *Adv. Funct. Mater.* **29**, 1806863 (2019).

48. Wang, D., Yang, J., He, P. & Zhou, H. A low-charge-overpotential lithium-CO$_2$ cell based on a binary molten salt electrolyte. *Energy Environ. Sci.* **14**, 4107–4114 (2021).

49. Feng, N. et al. Mechanism-of-action elucidation of reversible Li–CO$_2$ batteries using the water-in-salt electrolyte. *ACS Appl. Mater. Interfaces* **13**, 7396–7404 (2021).

50. Lu, Z. et al. A rechargeable Li–CO$_2$ battery based on the preservation of dimethyl sulfoxide. *J. Mater. Chem. A* **10**, 13821–13828 (2022).

51. Hou, Q. et al. CO$_2$-induced melting and solvation reconfiguration of phase-change electrolyte. *Adv. Mater.* **34**, 2202869 (2022).

52. Li, X., Qi, G., Zhang, J., Cheng, J. & Wang, B. Artificial solid-electrolyte interphase and bamboo-like N-doped carbon nanotube enabled highly rechargeable K-CO$_2$ batteries. *Adv. Funct. Mater.* **32**, 2105029 (2022).

53. Sánchez-Carrera, R. S. & Kozinsky, B. Computational Raman spectroscopy of organometallic reaction products in lithium and sodium-based battery systems. *Phys. Chem. Chem. Phys.* **16**, 24549–24558 (2014).

54. Zou, J. et al. Revisiting the role of discharge products in Li-CO$_2$ batteries. *Adv. Mater.* **35**, 2210671 (2023).

55. Zou, J. et al. Size-dependent effects of Ru nanoparticles on Li-CO$_2$ batteries. *ACS Energy Lett.* **9**, 5145–5155 (2024).

56. Li, Y. et al. Highly surface-wrinkled and N-doped CNTs anchored on metal wire: a novel fiber-shaped cathode toward high-performance flexible Li–CO$_2$ batteries. *Adv. Funct. Mater.* **29**, 1808117 (2019).

57. Qiao, Y. et al. Synergistic effect of bifunctional catalytic sites and defect engineering for high-performance Li–CO2 batteries. *Energy Storage Mater.* **27**, 133–139 (2020).

58. Zhuo, Z. et al. Cycling mechanism of Li$_2$MnO$_3$: Li–CO$_2$ batteries and commonality on oxygen redox in cathode materials. *Joule* **5**, 975–997 (2021).

59. Liu, B. et al. Recent advances in understanding Li–CO$_2$ electrochemistry. *Energy Environ. Sci.* **12**, 887–922 (2019).

60. Chen, J. et al. Electrolyte design for LiF-rich solid–electrolyte interfaces to enable high-performance microsized alloy anodes for batteries. *Nat. Energy* **5**, 386–397 (2020).

61. Li, T., Zhang, X. Q., Shi, P. & Zhang, Q. Fluorinated solid-electrolyte interphase in high-voltage lithium metal batteries. *Joule* **3**, 2647–2661 (2019).

62. Yang, Y., Wang, H., Zhu, C. & Ma, J. Armor-like inorganic-rich cathode electrolyte interphase enabled by the penta-fluorophenylboronic acid additive for high-voltage Li|| NCM622 batteries. *Angew. Chem.* **135**, 202300057 (2023).

63. Bai, P. et al. Formation of LiF-rich cathode-electrolyte interphase by electrolyte reduction. *Angew. Chem. Int. Ed.* **61**, e202202731 (2022).

64. Qiu, C. D. et al. Engineering peculiar cathode electrolyte interphase toward sustainable and high-rate Li–S batteries. *Adv. Energy Mater.* **13**, 2300229 (2023).

65. Sina, M. et al. Structural phase transformation and Fe valence evolution in FeO$_x$F$_{2-x}$/C nanocomposite electrodes during lithiation and de-lithiation processes. *J. Mater. Chem. A* **1**, 11629–11640 (2013).

66. Ward, J. D. et al. Identifying anthropogenic uranium compounds using soft X-ray near-edge absorption spectroscopy. *Spectrochim. Acta Part B: At. Spectrosc.* **127**, 20–27 (2017).

67. Yan, C. et al. Regulating the inner Helmholtz plane for stable solid electrolyte interphase on lithium metal anodes. *J. Am. Chem. Soc.* **141**, 9422–9429 (2019).

68. Luo, J. et al. Stable zinc anode solid electrolyte interphase via inner Helmholtz plane engineering. *Nat. Commun.* **15**, 6471 (2024).

69. Ma, S. et al. Modulating the inner Helmholz plane towards stable solid electrolyte interphase by anion-π interactions for high-performance anode-free lithium metal batteries. *Angew. Chem.* **137**, e202412955 (2025).

Acknowledgements

Author contributions

F.Z. conceived the idea, performed the experiments, and drafted the original manuscript. J.A.Y. and R.Z. conducted the theoretical calculations and MD simulations. L.T. conducted soft-XAS characterizations for positive electrodes and analysed the data. S.X. contributed to the electrolyte characterizations. L.C. performed the DEMS measurement and provided English editing. W.Z. and Z.G. directed the project and revised the paper.

Competing interests

The authors declare no competing interests.

Additional information

Supplementary information The online version contains supplementary material available at https://doi.org/10.1038/s41467-025-64369-z.

Correspondence and requests for materials should be addressed to Wenchao Zhang or Zaiping Guo.

Peer review information *Nature Communications* thanks the anonymous reviewer(s) for their contribution to the peer review of this work. [A peer review file is available].

Reprints and permissions information is available at http://www.nature.com/reprints

Publisher's note Springer Nature remains neutral with regard to jurisdictional claims in published maps and institutional affiliations.